

# Enhanced Energy Storage Density and Efficiency of Lead-Free $\text{Bi}_{0.5}\text{Na}_{0.5}\text{TiO}_3\text{-SrTiO}_3$ Ferroelectric Ceramics by $\text{BaZrO}_3$ Doping

Thi Hinh Dinh<sup>1,2,\*</sup>, Vu Diem Ngoc Tran<sup>3</sup>, Thi Thao Nguyen<sup>3</sup>  
Vinh Le Van<sup>1,2</sup>, Ky Nam Pham<sup>4</sup>

<sup>1</sup>Phenikaa University, Hanoi, Vietnam

<sup>2</sup>Phenikaa Research and Technology Institute, Hanoi, Vietnam

<sup>3</sup>Hanoi University of Science and Technology, Hanoi, Vietnam

<sup>4</sup>Viettel Aerospace Institute - Viettel Group, Hanoi, Vietnam

\*Email: hinh.dinhthi@phenikaa-uni.edu.vn

## Abstract

To improve the energy storage density and efficiency of lead-free ferroelectric ceramics, the ternary  $\text{Bi}_{0.5}\text{Na}_{0.5}\text{TiO}_3\text{-SrTiO}_3\text{-BaZrO}_3$  ferroelectric system was studied. All ceramics were fabricated by a conventional solid-state reaction method and sintered at 1150 °C for 2 h. The crystal structure, electric-field-induced polarization, energy storage density, and efficiency properties of all samples were analyzed. The X-ray diffraction patterns show that the addition of  $\text{BaZrO}_3$  in the  $\text{Bi}_{0.5}\text{Na}_{0.5}\text{TiO}_3\text{-SrTiO}_3$  system influences a phase transition from tetragonal to a pseudocubic structure. The electric field-induced-polarization loops confirm the phase transition from ferroelectric to relaxor in  $\text{Bi}_{0.5}\text{Na}_{0.5}\text{TiO}_3\text{-SrTiO}_3\text{-BaZrO}_3$  ceramics, which increases the energy storage density and efficiency of the samples. The energy storage density and efficiency of pure  $\text{Bi}_{0.5}\text{Na}_{0.5}\text{TiO}_3\text{-SrTiO}_3$  ( $x = 0$ ) were  $\sim 0.2 \text{ J/cm}^3$  and  $\sim 29\%$ . The addition of 1%  $\text{BaZrO}_3$  increases the energy storage density and efficiency of the sample to  $\sim 0.4 \text{ J/cm}^3$  and  $\sim 74\%$ . The further increase in the  $\text{BaZrO}_3$  content to  $x = 0.03$  shows the energy storage density of  $\sim 0.38 \text{ J/cm}^3$  with an energy storage efficiency of  $\sim 97\%$ . The results indicate promising lead-free ferroelectric ceramic candidates for energy storage capacitor applications.

Keywords: Ferroelectrics, energy storage density, energy storage efficiency, electroceramics, BNT.

## 1. Introduction

Nowadays, the world is facing energy and environmental issues caused by the gradual exhaustion of fossil fuels. The development of clean and renewable energy technologies has become a global priority. Some renewable energy technologies such as wind energy, wave energy, or solar energy have been explored. However, these energies are heavily dependent on energy storage units due to their intermittent nature. The lead-free ceramic capacitors, recently, have been widely studied due to their advantageous applications for energy storage in pulsed-power and power-conditioning electronic devices [1]. In comparison with batteries, fuel cells, and supercapacitors, lead-free ceramic capacitors present high power densities, rapid charge/discharge rate, and long cycle lifetime. However, the energy density values of ceramic capacitors are usually lower than that in supercapacitors or batteries [1]. Therefore there is a great need to develop new lead-free ceramics with high energy storage density and high energy storage efficiency. These lead-free ceramics can be made of dielectrics, ferroelectrics, and anti-ferroelectrics materials [2].

Bismuth sodium titanate ( $\text{Bi}_{0.5}\text{Na}_{0.5}\text{TiO}_3$ , BNT) is one of the most important and superior lead-free ferroelectrics materials discovered by Smolenskii and

co-authors [3]. BNT ceramic is  $A$ -site complex perovskites of the form  $(A1,A2)\text{BO}_3$ , where the  $\text{Bi}^{3+}$  and  $\text{Na}^+$  ions sit on the  $A$ -site, while  $\text{Ti}^{4+}$  ion occupies the  $B$ -site of the perovskite unit cell. At room temperature, BNT ceramic has a rhombohedral crystal structure with  $a = 3.98 \text{ \AA}$  and  $\alpha = 98.67^\circ$  [4] and undergoes a diffuse phase change to tetragonal at a Curie temperature ( $T_c$ ) of 320 °C [5]. BNT ceramic is also considered to be relaxors and thus the dielectric constant versus temperature relationship is strongly frequency-dependent [6]. BNT ceramic shows strong ferroelectric with a significant remnant polarization of  $38 \mu\text{C/cm}^2$  and a coercive field ( $E_c$ ) of 7.3 kV/mm [7], a property that is not often reported in high mechanical bending strength.

Among some lead-free BNT-based ferroelectric ceramics, the  $\text{Bi}_{0.5}\text{Na}_{0.5}\text{TiO}_3\text{-SrTiO}_3$  (BNST) ceramic becomes one of the most interesting materials in lead-free ceramics due to their large electric-field-induced strain properties under a low applied electric field [8]. The BNST ceramics was firstly reported by a Japanese group at Tokyo University of Science in 2018 [9]. However, it get more attention since the German group in Technische Universitat Darmstadt found the core-shell structure in 0.75BNT-0.25ST ceramic in 2015 [10]. The core-shell structure in 0.75BNT-0.25ST ceramic presents a greater normalized strain

( $S_{\max}/E_{\max}$ ) than that in BNT-based materials and close to the  $\text{Pb}(\text{Zr},\text{Ti})\text{O}_3$ -based ceramics in commercial PIC 151 [10]. However, most of the recent research of BNST-based ceramics focuses on the piezoelectric properties and there is a lack of studies on the energy storage density properties of BNST-based materials so far [2, 8]. Besides,  $\text{Ba}^{2+}$  ion was known as an effective modification to improve the energy storage densities of ferroelectric ceramics [2]. Therefore, this study focuses on the enhancement of the energy storage density of BNST ceramics by  $\text{BaZrO}_3$  doping. All samples were fabricated by a conventional solid-state reaction method. The crystal structures, electric-field-induced polarization, energy storage density, and energy storage efficiency properties of  $(0.75-x)\text{Bi}_{0.5}\text{Na}_{0.5}\text{TiO}_3-0.25\text{SrTiO}_3-x\text{BaZrO}_3$  (BNST-BZ100x) ceramics were analyzed.

## 2. Experiment

The properties of ceramic materials strongly depend on their chemical composition, processing routes, and fabrication techniques. To achieve greater performance and reliability of ceramics, it is important to handle the compositions and processes parameters very carefully. In the development and production of more advanced ceramics, extraordinary control of the materials and processing minimize structural and microstructure defects. The ceramics used in this study were fabricated by a conventional solid-state reaction method and the experimental procedure was carried out as shown in Fig. 1.

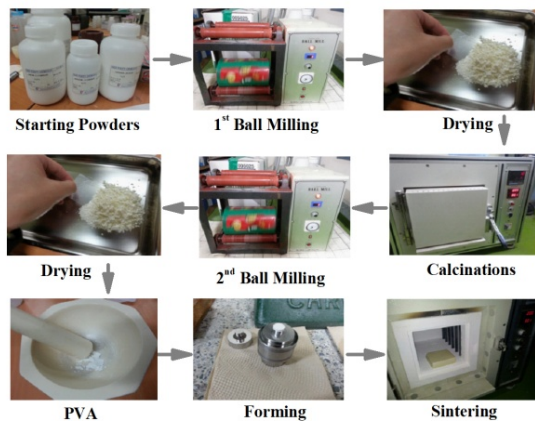


Fig. 1. Conventional solid-state reaction method for BNST-BZ100x piezoelectric ceramics.

### 2.1. Compositions

The chemical formulations of the ceramics is  $(0.75-x)\text{Bi}_{0.5}\text{Na}_{0.5}\text{TiO}_3-0.25\text{SrTiO}_3-x\text{BaZrO}_3$  with  $x = 0; 0.01; 0.03$ , abbreviated as BNST-BZ100x. The conditions and sequences used in the sample preparation, characterization and testing are given in the following sections.

### 2.2. Raw Materials

Commercially available reagent grade Bismuth (III) Oxide ( $\text{Bi}_2\text{O}_3$ ), Sodium Carbonate ( $\text{Na}_2\text{CO}_3$ ), Strontium Carbonate ( $\text{SrCO}_3$ ), Titanium (IV) Oxide ( $\text{TiO}_2$ ), Barium Carbonate ( $\text{BaCO}_3$ ), and Zirconium (IV) oxide ( $\text{ZrO}_2$ ) were used as the starting raw materials in the fabrication of the mentioned three systems. The detailed specifications of these powders are given in Table 1. These starting materials were first put in the oven at  $100\text{ }^\circ\text{C}$  for 24 h to remove moisture and then weighed according to their stoichiometric formula.

Table 1. Raw materials

Chemical Name	Source
Bismuth (III) oxide $\text{Bi}_2\text{O}_3$	99.95%, High Purity Chemicals, Japan
Sodium Carbonate $\text{Na}_2\text{CO}_3$	99.95%, High Purity Chemicals, Japan
Strontium Carbonate $\text{SrCO}_3$	99.95%, High Purity Chemicals, Japan
Titanium (IV) Oxide $\text{TiO}_2$	99.95%, High Purity Chemicals, Japan
Barium Carbonate $\text{BaCO}_3$	99.95%, High Purity Chemicals, Japan
Zirconium (IV) Oxide $\text{ZrO}_2$	99.95%, High Purity Chemicals, Japan

### 2.3. Mixing and Milling

After weighing the starting raw powders according to their stoichiometric formula, they were mixed and milled thoroughly inside a polyethylene jar with  $\text{ZrO}_2$  balls (5-10 mm in diameter) as a mixing media and ethanol as a solvent for 24 h, at the rate of 300 rpm. During the milling process, when ball and ball or ball and jar wall collide, some amount of powder between them is repeatedly fractured, cold-welded, flattened, and re-welded, which reduces the particle size and forms uniform particles slurry. The wet slurry is then dried at  $100\text{ }^\circ\text{C}$  for 24 h.

### 2.4. Calcination

After proper mixing and milling, the dried milled powders were calcined at  $850\text{ }^\circ\text{C}$  for 2 h in a closed alumina crucible with an indigenous programmable furnace. The powders were thoroughly grounded using mortar and passel and ball-milled again to avoid glamorization of the particles. The pulverized powders were then used for the study of their phase formation as well as their reaction mechanism.

### 2.5. Pellet Preparation

After calcinations, the powders were added to an organic binder polyvinyl alcohol (PVA, 5%) and ground and dried again at 100 °C for 1 h. To get uniform and fined grain, the granules were passed through a 180 μm sieve. Pellets of 0.4 and 0.6g were made by using a cylindrical steel die of 10 mm in diameter. Initially, the die was kept in a highly viscous mobile oil to prevent it from rusting. Taking out from the oil, the die was cleaned with isopropyl alcohol and acetone. Then the die containing the powder was uniaxially pressed with a pressure of 98 Mpa in a hydraulic press. Before releasing the pressure from the die, a minimum of 10 seconds was given to minimize the stress on the pellet.

### 2.6. Sintering

The density of the electronic ceramics is a very sensitive parameter and that directly affects the material properties. Therefore, proper sintering of the pellets is essential for electrical property measurements. The pellets of the prepared compositions were put in an alumina crucible and the corresponding powders were used as ambient to prevent Bi<sup>3+</sup> and Na<sup>+</sup> evaporation from the pellets during high sintering temperature. The sintering conditions of the pellets are at 1150 °C for 2 h in a programmable furnace. After the sintering process, the samples were furnace cooled and taken out of the furnace for density measurements.

## 3. Characterization

### 3.1. Density

The density of the sintered ceramic pellet was measured by using Archimedes' immersion principal method using an Electronic Densimeter (SD-120L). First, the mass of the pellets was measured and then the sample was immersed in DI water, where it displaced an amount of water equal to its volume and its weight is diminished by the weight of the liquid displaced. The density was calculated by below equation:

$$\rho = \frac{W_{dry}}{W_{dry} - W_{liquid}} \text{ (g/cm}^3\text{)} \quad (1)$$

where:

$W_{dry}$  is the dry weight of the sample;

$W_{liquid}$  is the weight of the sample in water;

### 3.2. X-ray Diffraction Analysis

X-ray diffraction (XRD) technique is a powerful tool for material characterization as well as for detailed structural elucidation. As the physical properties of solids (e. g., electrical, optical, magnetic, ferroelectric, etc.) depend on atomic arrangements of materials, determination of the crystal structure is an indispensable part of the characterization of materials,

mainly in the identification of the chemical species. In the present study crystallographic and phase analyses were performed by an X-ray diffractometer (XRD RAD III, Rigaku, Japan) by using monochromatic CuK<sub>α</sub> radiation with the wavelength  $\lambda_{K\alpha}=1.54178 \text{ \AA}$ . The detection range was 25° to 65° with a step size of 0.02° and a speed of 2°/min. The crystal parameters were calculated by using Bragg's law:

$$n\lambda = 2d \sin \theta \quad (2)$$

$$\frac{1}{d^2} = \frac{h^2 + k^2}{a^2} + \frac{l^2}{c^2} \quad (3)$$

where:

$$\lambda = \lambda_{K\alpha} = 1.54178 \text{ \AA}$$

$d$  is lattice spacing;

$\theta$  is diffraction angle;

$a$  and  $c$  are crystal parameters for tetragonal structure. For rhombohedra or pseudocubic,  $a = c$ ;

$h$ ,  $k$ , and  $l$  are lattice indexes.

The theoretical density of ceramic material was calculated by equation [11].

$$\rho = \frac{n(\sum A_C + \sum A_A)}{V_C N_A} \quad (4)$$

where:

$\rho$ : is the X-ray density (g/cc);

$n$  is the number of formula units within the unit cell

$\sum A_C$ : is the sum of the atomic weights of all cations in the formula unit

$\sum A_A$ : is the sum of the atomic weights of all anions in the formula unit

$V_C$ : is the unit cell volume

$N_A$  is Avogadro's number,  $N = 6.02214076 \times 10^{23}$  formula units/mol;

### 3.3. Electric Field-Induced-Polarization (P-E) Hysteresis Loops

To make a fine, smooth, and flat surface for subsequent electrical property measurements, lapping was carried out to obtain 1 mm thick specimens of the sintered pellets by lapping machine (HRG-150E). The lapped pellets were then washed in acetone, polished with sandpaper (cc 800 cw), and then with an electric polishing machine (Dong ILT, 802-0408). The polished pellets were then thoroughly sonicated with acetone in the ultrasonic machine (Branson, 5210) and dried at 100 °C for 5 h.

After the lapping process, the selection of suitable electrodes for the test of materials is important to get a good response of the test material. The mixed

of Platinum (Pt) and silver (Ag) electrodes were deposited on the opposite faces of the lapped and polished pellets by direct current sputtering and screen printing techniques. The deposited electrodes were then fired at 700 °C for 30 min.

The electrode samples are composed of randomly oriented grains, which possess identical structures but have a random orientation, resulting in a small or zero net spontaneous polarization. Therefore, it can be supposed that the properties of samples are isotropic. A high external electric field is usually applied to ferroelectric ceramic to get a piezoelectric effect, so-called poling. The net polarization is then not zero, as the dipoles of each grain tend to align themselves in the direction of the applied electric field. In this work, ceramic samples with 1 mm thickness were poled under an applied electric field of 4 kV/mm by a high voltage power supply (Conver tech, SHV30) in a silicon oil bath at room temperature.

The electric field-induced-polarization ( $P$ - $E$ ) hysteresis loops in this study were taken at 0.3 Hz and maximum applied field ( $E_{\max}$ ) of 4 kV/mm with a 15- $\mu$ F measurement capacitance by a modified Sawyer-Tower circuit equipped with an optical sensor (Philtec, Inc., Annapolis, MD, USA).

### 3.4. Storage Energy Density and Efficiency

The energy storage density and energy loss of a sample can be evaluated by integrating the area between the polarization axis and the charge/discharge curve based on the  $P$ - $E$  loop as seen in Fig. 2.

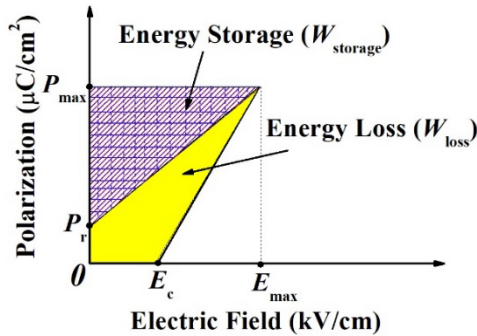


Fig. 2. Energy storage density and energy loss during the charge-discharge process [2].

The volumetric energy density ( $W$ ), energy storage density ( $W_{\text{storage}}$ ), energy loss ( $W_{\text{loss}}$ ), and the energy storage efficiency ( $\eta$ ) are determined utilizing the following equations [2]:

$$W = \int_0^{P_{\max}} E dP \quad (5)$$

$$W_{\text{storage}} = \int_{P_r}^{P_{\max}} E dP \quad (6)$$

$$W_{\text{loss}} = W - W_{\text{storage}} \quad (7)$$

$$\eta = \frac{W_{\text{storage}}}{W} \times 100\% \quad (8)$$

where:

$E$  is the applied electric field;

$dP$  is the change of polarization in the material induced by the applied electric field;

$P_{\max}$  is maximum polarization;

$P_r$  is remnant polarization.

## 4. Results and Discussions

### 4.1. Crystal Structures

Fig. 3 presents the  $X$ -ray diffraction patterns of BNST-BZ100 $x$  ceramics. All samples have a typical  $ABO_3$  perovskite structure without any evidence of secondary phases. The results suggest that BNST has allowed all  $Ba^{2+}$  and  $Zr^{4+}$  ions to enter the host lattice to form a homogeneous solid solution. To further clarify the effect of  $BaZrO_3$  content on the phase structure of BNST ceramic, fine scanning XRD patterns were recorded in the  $2\theta$  range of 38.5°-47.5°, as shown in Fig. 3(b).

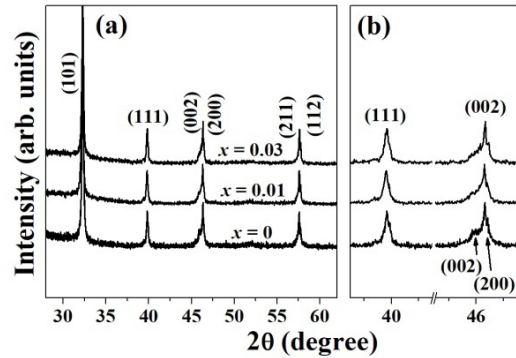


Fig. 3. XRD patterns of the sintered BNST-BZ100 $x$  ceramics as a function of  $BaZrO_3$  content ( $x$ ).

The single (111) peak at  $2\theta \sim 40^\circ$  and the splitting (002)/(200) peaks at  $2\theta \sim 46^\circ$  corresponding to a tetragonal structure were found for pure BNST ( $x = 0$ ) sample. The results are consistent with the previous reports on (1- $x$ )BNT- $x$ ST ceramics in which a morphotropic phase boundary (MPB) was reported to exist in the composition range of  $x = 0.26$ - $0.28$  [9]. It is interesting to note that the addition of  $BaZrO_3$  induces the tetragonal-pseudocubic phase transition, resulting in single (111) and single (002) peaks at  $2\theta \sim 40^\circ$  and  $2\theta \sim 46^\circ$  for  $x > 0$  samples, respectively. The ionic radius of  $Ba^{2+}$  ( $R_{Ba} = 1.61 \text{ \AA}$ ) is larger than the average ionic radius of the  $A$ -size ( $R_{Bi} = 1.36 \text{ \AA}$ ,  $R_{Na} = 1.39 \text{ \AA}$ ,  $R_{Sr} = 1.44 \text{ \AA}$ ) and the ionic radius of  $Zr^{4+}$  ( $R_{Zr} = 0.72 \text{ \AA}$ ) is larger than the ionic radius of the

Ti<sup>4+</sup> ( $R_{Ti} = 0.605 \text{ \AA}$ ) in the *B*-size [12]. The increase in the symmetry of the BNST-BZ100 $x$  crystal is probably by shrinkage in the directions of *a* and *c* axes of the tetragonal lattice, which may be due to the difference in Shannon's effective ionic radius.

#### 4.2. Densities

The measured density (determined from Archimedes principle), the theoretical density (*X*-ray density), and the relative density (ratio of the measured density to the theoretical density) of the sintered samples were presented in Fig. 4. The  $x = 0$  sample has a measured density of  $5.62 \text{ g/cm}^3$  and a theoretical density of  $5.85 \text{ g/cm}^3$ . The addition of 0.01 mol BaZrO<sub>3</sub> content increases the measured density and the theoretical density of the sample to  $5.69 \text{ g/cm}^3$  and  $5.92 \text{ g/cm}^3$ . Further increase in BaZrO<sub>3</sub> content leads to a decrease in the densities of the sample, the  $x = 0.03$  ceramic has the measured density of  $5.65 \text{ g/cm}^3$  and the theoretical densities of  $5.91 \text{ g/cm}^3$ .

Table 2 presents the measured densities, theoretical densities, and the relative densities of the sintered BNST-BZ100 $x$  ceramics as a function of  $x$ . The relative densities of all sintered samples were more than 95%. It is well known that the measured density of a sintered sample is usually less and that can't exceed the theoretical density, because the macroscopic specimen usually contains some cracks and pores.

Table 2. Densities of BNST-BZ100 $x$  ceramics

$X$	Measured density (g/cm <sup>3</sup> )	Theoretical density (g/cm <sup>3</sup> )	Relative density (%)
0	56.2	58.5	96
0.01	56.9	59.2	96
0.03	56.5	59.1	95.4

#### 4.3. Electric Field-Induced-Polarization Hysteresis Loops

Fig. 5 presents the electric-field-induced-polarization hysteresis loops of BNST-BZ100 $x$  ceramics at 4 kV/mm. The addition of BaZrO<sub>3</sub> changes the shape of the *P*-*E* loops and reduces the maximum polarization ( $P_{\max}$ ), remnant polarization ( $P_r$ ), and the coercive field ( $E_c$ ) values. The *P*-*E* loops confirm the phase transition from ferroelectric to relaxor phase as a function of BaZrO<sub>3</sub> content.

The corresponding  $P_{\max}$ ,  $P_r$ , and  $E_c$  values are presented in Fig. 6 and Table 3. Compared to the significant decrease in the  $P_r$ , the  $P_m$  shows a slight change, which may depend on the relationship between the electric-field-induced polarization and the long-range ferroelectric ordered. The  $P_m$  is mostly related to the poled state of the long-range ferroelectric

ordered state while the  $P_r$  is associated with the stability of such a long-range ferroelectric ordered state. Therefore, the addition of BaZrO<sub>3</sub> breaks the long-range order as the ferroelectric (FE) in BNST ceramic to form the polar nano regions (PNRs) as the relaxor phase, resulting in a sharp decrease in the  $P_r$  value.

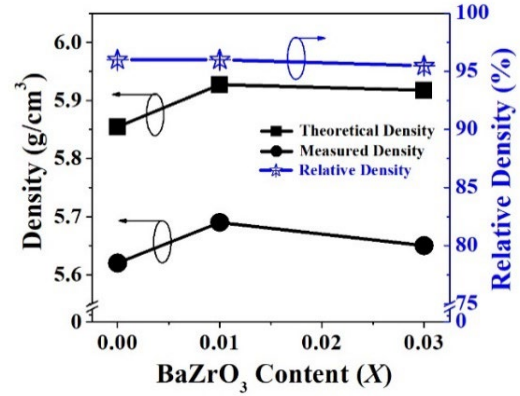


Fig. 4. Densities of the sintered BNST-BZ100 $x$  ceramics as a function of BaZrO<sub>3</sub> content ( $x$ ).

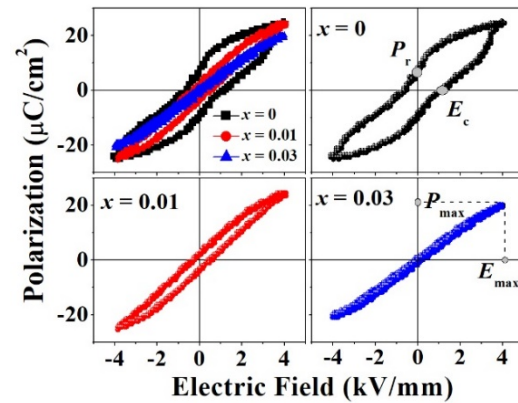


Fig. 5. *P*-*E* loops of BNST-BZ100 $x$  ceramics as a function of BaZrO<sub>3</sub> content ( $x$ ).

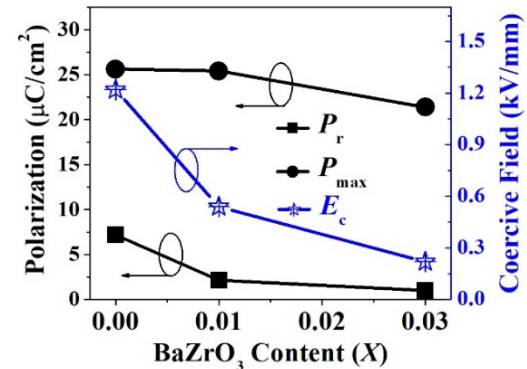


Fig. 6.  $P_{\max}$ ,  $P_r$ , and  $E_c$  of BNST-BZ100 $x$  ceramics as a function of BaZrO<sub>3</sub> content ( $x$ ).

Table 3. Ferroelectric properties of the samples

$X$	$P_{\max}$ ( $\mu\text{C}/\text{cm}^2$ )	$P_r$ ( $\mu\text{C}/\text{cm}^2$ )	$E_c$ (kV/mm)
0	25.6	7.17	12.2
0.01	25.4	2.14	5.4
0.03	21.4	0.5	1.2

#### 4.4. Storage Energy Density and Efficiency

To evaluate the potential application of the BNST-BZ100 $x$  ceramics for capacitive storage systems, the energy density is directly calculated from the  $P$ - $E$  hysteresis loops. The volumetric energy density ( $W$ ) is calculated by integrating the area between the charge curve and the polarization axis based on (5) as seen in Fig. 7.

The recoverable energy density or energy storage density ( $W_{\text{storage}}$ ) of a ferroelectric ceramic is calculated by integrating the area between the discharge curve and the polarization axis based on (6) as seen in Fig. 8. The energy loss ( $W_{\text{loss}}$ ) and energy storage efficiency ( $\eta$ ) are also calculated based on (7) and (8).

Table 4. Energy densities of the samples

$X$	$W$ ( $\text{J}/\text{cm}^3$ )	$W_{\text{storage}}$ ( $\text{J}/\text{cm}^3$ )	$\eta$ (%)
0	0.69	0.20	29.19
0.01	0.54	0.40	74.03
0.03	0.39	0.38	97.66

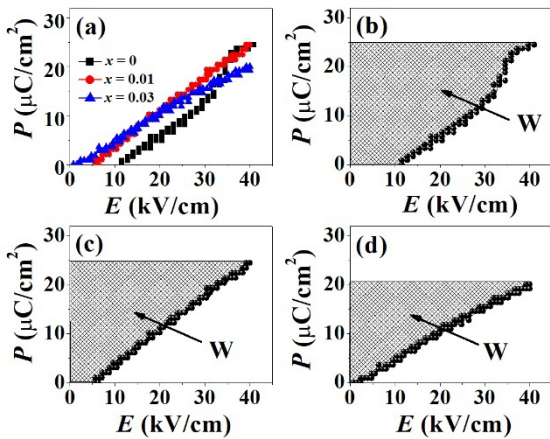


Fig. 7.  $W$  of BNST-BZ100 $x$  ceramics: (a) all samples, (b)  $x = 0$ , (c)  $x = 0.01$ , and (d)  $x = 0.03$ .

Fig. 9 presents the  $W$ ,  $W_{\text{storage}}$ ,  $W_{\text{loss}}$ , and  $\eta$  of BNST-BZ100 $x$  ceramics under an applied electric field of 4 kV/mm. The addition of BaZrO<sub>3</sub> reduces the

$W$  and  $W_{\text{loss}}$ , however enhances the  $W_{\text{storage}}$  and the  $\eta$  values. The  $W_{\text{storage}}$  of BNST sample is  $\sim 0.20 \text{ J}/\text{cm}^3$ . The addition of BaZrO<sub>3</sub> increases the  $W_{\text{storage}}$  to  $\sim 0.4 \text{ J}/\text{cm}^3$  for  $x = 0.01$  and  $0.38 \text{ J}/\text{cm}^3$  for  $x = 0.03$  samples. Besides, the energy loss of the ceramics was decreased as a function of BaZrO<sub>3</sub> content, and the corresponding energy storage efficiency was increased from  $\sim 29\%$  for  $x = 0$  to  $\sim 74\%$  for  $x = 0.01$  and finally it is  $\sim 97\%$  for  $x = 0.03$  samples. The detailed results are shown in Table 4.

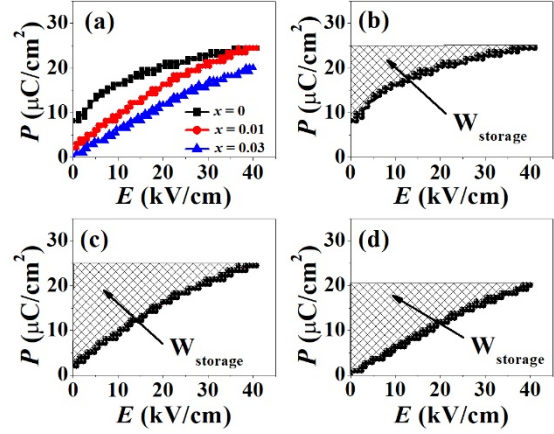


Fig. 8.  $W_{\text{storage}}$  of BNST-BZ100 $x$  ceramics: (a) all samples, (b)  $x = 0$ , (c)  $x = 0.01$ , and (d)  $x = 0.03$ .

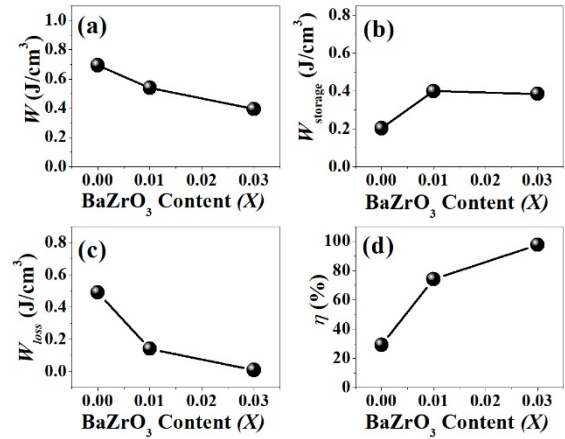


Fig. 9. (a)  $W$ , (b)  $W_{\text{storage}}$ , (c)  $W_{\text{loss}}$ , and (d)  $\eta$  of BNST-BZ100 $x$  ceramics as a function of BaZrO<sub>3</sub> content ( $x$ ).

To explain the improvement of the energy density and efficiency in BZ-doped BNST ceramics, the energy storage schematic representation of pure BNST and 1%BZ-doped BNST are presented in Fig. 10 and Fig. 11. Initially, BNST ceramic is a ferroelectric with a tetragonal structure and a typical ferroelectric characteristic  $P$ - $E$  loop (large  $P_r$  and large  $E_c$ ) as seen in Fig. 10. The PNRs in BNST ceramic are randomly oriented at state (I) when  $E = E_c$  and  $P = 0$ . During the charging process from state (I) to state (II), the PNRs were gradually changed to FE. At state (II), all the FE were oriented under an applied electric field

and the polarization reaches maximum. Besides, the oriented FE in state (II) was still oriented FE at state (III) during the discharge process because of the irreversible behaviors of FE in ferroelectric materials [8]. Therefore, the energy storage density of BNST is low due to the small difference in polarization values of  $P_{\max}$  and  $P_r$  in the sample.

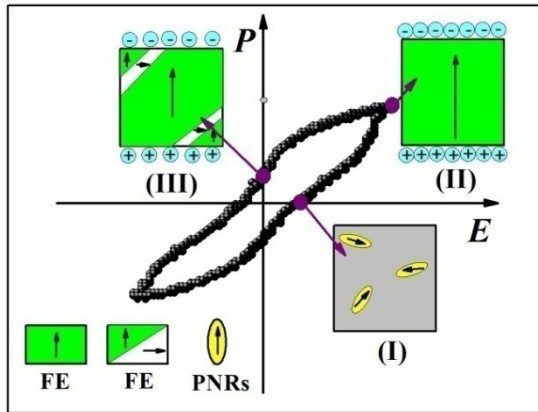


Fig. 10. Energy storage schematic representation of BNST ceramic.

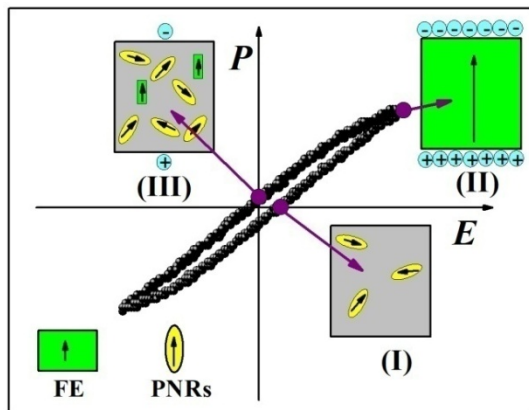


Fig. 11. Energy storage schematic representation of BNST-BZ1 ceramic.

For 1%BZ-doped BNST sample, the PNRs was exhibited at state (I), FE was found at state (II) and the mixture of FE and PNRs were observed in state (III), as seen in Fig. 11. Therefore the large energy storage density in BNST-BZ1 was generated due to the big difference in polarization values of  $P_{\max}$  and  $P_r$ .

## 5. Conclusion

Lead-free  $(0.75-x) \text{Bi}_{0.5}\text{Na}_{0.5}\text{TiO}_3-0.25\text{SrTiO}_3-x\text{BaZrO}_3$  with  $x = 0; 0.01; 0.03$  ceramics were successfully fabricated by the conventional solid-state reaction method. The X-ray diffraction patterns confirm the phase transition from tetragonal to a pseudocubic structure as a function of  $\text{BaZrO}_3$  content in the BNST-BZ100x ceramics. The electric-field-induced polarization hysteresis loops suggest the ferroelectric behavior in the BNST sample while the

relaxor behavior was seen in the  $\text{BaZrO}_3$ -doped BNST ceramics. The results confirm that the breaking of long-range ferroelectric order in BNST ceramic occurred by the addition of BZ can improve the energy storage density. Interestingly, the energy storage of  $0.38 \text{ J/cm}^3$  with an efficiency of 97% was found in the  $x = 0.03$  sample, showing a potential lead-free ferroelectric ceramic for energy storage capacitor applications.

## Acknowledgments

This research is funded by Vietnam National Foundation for Science and Technology Development (NAFOSTED) under grant number 103.02-2020.28.

## References

- [1] H. Palneedi, M. Peddigari, G.T. Hwang, D.Y. Jeong, J. Ryu, High-performance dielectric ceramic films for energy storage capacitors: progress and outlook, *Adv. Funct. Mater.*, vol. 28, no. 42, pp.1803665, Oct. 2018. <https://doi.org/10.1002/adfm.201803665>
- [2] Z. Yang, H. Du, L. Jin, D. Poelman, High-performance lead-free bulk ceramics for electrical energy storage applications: design strategies and challenges, *J. Mater. Chem. A*, vol. 9, pp.18026-18085, Jul. 2021. <https://doi.org/10.1039/D1TA04504K>
- [3] G.A. Smolenskii, V.A. Isupov, A.I. Agranivskaya, N.N. Krainik, New ferroelectrics of complex composition. IV, *Sov. Phys. Sol. St.* Vol. 2, pp. 2651-2654, 1961.
- [4] V.A. Isupov, Ferroelectric  $\text{Na}_{0.5}\text{Bi}_{0.5}\text{TiO}_3$  and  $\text{K}_{0.5}\text{Bi}_{0.5}\text{TiO}_3$  perovskites and their solid solutions, *Ferroelectrics*, vol. 315, no. 1, pp. 123-147, Dec. 2005. <https://doi.org/10.1080/001501990910276>
- [5] I.P. Pronin, P.P. Symnikov, V.A. Isupov, V.M. Egorov, N.V. Zaitseva, Peculiarities of phase transitions in sodium-bismuth titanate, *Ferroelectrics*, vol. 25, no. 1, pp. 395-397, 1980. <https://doi.org/10.1080/00150198008207029>
- [6] L.E. Cross, Relaxor ferroelectrics, *Ferroelectrics*, vol. 76, no. 1, pp. 241-267, 1987. <https://doi.org/10.1080/00150198708016945>
- [7] H. Nagata, N. Koizumi, T. Takenaka, Lead-free piezoelectric ceramics of  $(\text{Bi}_{1/2}\text{Na}_{1/2})\text{TiO}_3\text{-BiFeO}_3$  system, *Key Eng. Mater.*, vol. 169, pp. 37-40, Jan. 1999. <https://doi.org/10.4028/www.scientific.net/KEM.169-170.37>
- [8] S. Zhang, B. Malic, J.F. Li, J. Rödel, Lead-free ferroelectric materials: Prospective applications, *J. Mater. Res.*, vol. 36, no. 5, pp. 985-995, Mar. 2021. <https://doi.org/10.1557/s43578-021-00180-y>
- [9] Y. Hiruma, Y. Imai, Y. Watanabe, H. Nagata, T. Takenaka, Large electrostrain near the phase transition temperature of  $(\text{Bi}_{0.5}\text{Na}_{0.5})\text{TiO}_3\text{-SrTiO}_3$  ferroelectric ceramics, *Appl. Phys. Lett.*, vol. 92, no. 26, pp. 262904 (3 pages), Jun. 2008. <https://doi.org/10.1063/1.2955533>

- [10] M. Acosta, L.A. Schmitt, L.M. Luna, M.C. Scherrer, M. Brilz, K.G. Webber, M. Deluca, H.J. Kleebe, J. Rödel, M. Donner, Core-shell lead-free piezoelectric ceramics: current status and advanced characterization of the  $\text{Bi}_{1/2}\text{Na}_{1/2}\text{TiO}_3\text{-SrTiO}_3$  system, *J. Am. Ceram. Soc.*, vol 98, no. 11, pp. 3405-3422, Nov. 2015.  
<https://doi.org/10.1111/jace.13853>
- [11] W.D. Callister Jr, D. G. Rethwisch, *Materials Science and Engineering: An Introduction*, 9<sup>th</sup> Edition, Wiley, 2014, pp. 476.
- [12] R.D. Shannon, Revised effective ionic radii and systematic studies of interatomic distances in halides and chalcogenides, *Acta Cryst. A*, vol 32, pp. 751-767, 1976.  
<https://doi.org/10.1107/S0567739476001551>